In-plane Wilson loop for measurement of quantized non-Abelian Berry flux

Alexander C. Tyner,[1,*] Shouvik Sur,[2,†] Qunfei Zhou,[3,4,‡] Danilo Puggioni,[5] Pierre Darancet,[4,6] James M. Rondinelli,[1,5,6] and Pallab Goswami[1,2,§]

[1]*Graduate Program in Applied Physics, Northwestern University, Evanston, Illinois 60208, USA*
[2]*Department of Physics and Astronomy, Northwestern University, Evanston, Illinois 60208, USA*
[3]*Materials Research Science and Engineering Center, Northwestern University, Evanston, Illinois 60208, USA*
[4]*Center for Nanoscale Materials, Argonne National Laboratory, Argonne, Illinois 60439, USA*
[5]*Department of Materials Science and Engineering, Northwestern University, Evanston, Illinois 60208, USA*
[6]*Northwestern Argonne Institute for Science and Engineering, Evanston, Illinois 60208, USA*

(Received 27 February 2024; revised 24 April 2024; accepted 29 April 2024; published 15 May 2024)

Band topology of anomalous quantum Hall insulators can be precisely addressed by computing the Chern numbers of constituent nondegenerate bands, describing the presence of quantized, Abelian Berry flux through the two-dimensional Brillouin zone. Can Berry flux be captured for the $SU(2)$ Berry connection of two-fold degenerate bands in spinful materials preserving space-inversion ($\mathcal{P}$) and time-reversal ($\mathcal{T}$) symmetries without detailed knowledge of underlying basis? We address this question by investigating the correspondence between a non-Abelian generalization of Stokes' theorem and the manifestly gauge-invariant eigenvalues of Wilson loops computed along in-plane contours which preserve the underlying crystalline symmetry. The importance of this correspondence is elucidated by performing natural number resolved classification of *ab initio* band structures of three-dimensional, Dirac materials. Our work underscores how identification of quantized Berry flux, both Abelian and non-Abelian, offers a unified framework for addressing first-order and higher-order topology of insulators and semimetals.

DOI: 10.1103/PhysRevB.109.195149

I. INTRODUCTION

The basic concepts of topological band theory were developed by considering global properties of nondegenerate energy bands of time-reversal symmetry breaking, two-dimensional insulators [1–9]. The band eigenfunctions of such systems are determined up to arbitrary complex phase factors, i.e., $\psi_n(\mathbf{k})$ and $e^{i\alpha_n(\mathbf{k})}\psi_n(\mathbf{k})$ are equally good candidate eigenfunctions for the nth band, with $n = 1, 2, 3, \ldots, N$. This U(1) redundancy for individual bands leads to Abelian Berry's connection, $\mathbf{A}_n(\mathbf{k}) = -i\langle\psi_n|\nabla|\psi_n\rangle$ and corresponding Berry's curvature $\mathbf{\Omega}_n(\mathbf{k}) = \nabla \times \mathbf{A}_n(\mathbf{k})$. By integrating $\mathbf{\Omega}_n^j$ over the two-dimensional Brillouin zone (BZ), one arrives at the quantized flux of U(1) curvature, $\int d^2k\mathbf{\Omega}_n(\mathbf{k}) = 2\pi C_n$, where C_n is the Chern number of band n. There exist many reliable methods for computing C_n. For example, by measuring the Berry's phase accrued by $\psi_n(\mathbf{k})$ when it is parallel transported along any nonintersecting closed contour and relating it to enclosed flux by Stokes theorem.

Can quantized flux exist for twofold degenerate bands of parity and time-reversal invariant systems with $\mathcal{T}^2 = -1$? The twofold degeneracy gives rise to local SU(2) redundancy of each band; as $\{\psi_{n,\uparrow}(\mathbf{k}), \psi_{n,\downarrow}(\mathbf{k})\}^T$, $e^{i\theta_n\hat{n}(\mathbf{k})\cdot\sigma}\{\psi_{n,\uparrow}(\mathbf{k}), \psi_{n,\downarrow}(\mathbf{k})\}^T$ are equally good candidate wave functions. The curvature, $F_{n,s,s'}$, of SU(2) Berry's connections, $\mathbf{A}_{n,s,s'}(\mathbf{k}) = -i\langle\psi_{n,s}(\mathbf{k})|\nabla|\psi_{n,s}(\mathbf{k})\rangle$, is gauge covariant. Therefore there are many conceptual subtleties in assigning gauge-invariant non-Abelian Berry's flux. If global symmetries such as U(1) spin-conservation [6] or mirror symmetry [10] are present, it becomes possible to assign a global spin quantization axis [U(1) gauge-fixing of SU(2) connections]. In the case of a mirror symmetry, one can separate the eigenspace into two subspaces, labeled by the eigenvalues of the mirror operator, and calculate C_n in each subspace.

In the absence of mirror or spin-rotation symmetry, it has been shown that the relative Chern number of individual Kramers pairs and the occupied subspace of a spinful, $\mathcal{T}$-preserving system may still be accomplished by projecting into nondegenerate, Abelian subspaces. This is done through construction of the projected spin operator (PSO), $P(\mathbf{k})\hat{s}P(\mathbf{k})$, where $P(\mathbf{k})$ is the projector onto occupied bands and $\hat{s}$ is a preferred (pseudo)spin-quantization axis [11,12]. In the absence of spin-orbit coupling (presence of U(1)-spin conservation law) the eigenvalues of the PSO are fixed as ± 1; when spin-orbit coupling is introduced the eigenvalues are no longer

*Current address: Nordita, KTH Royal Institute of Technology and Stockholm University 106 91 Stockholm, Sweden; alexander-tyner2022@u.northwestern.edu

†Current address: Department of Physics and Astronomy, Rice Center for Quantum Materials, Rice University, Houston, TX 77005, USA.

‡Current address: Department of Physics and Astronomy, University of Kansas, Lawerence, KS, USA.

§Corresponding author: pallab.goswami@northwestern.edu

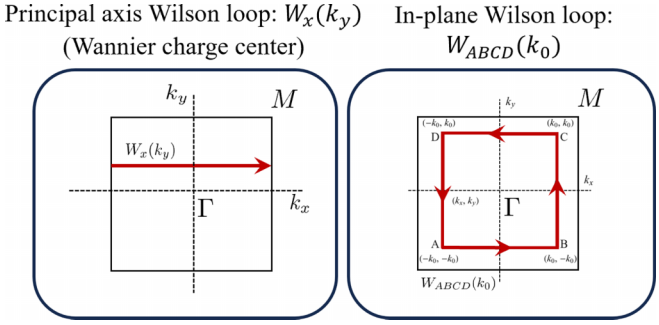

FIG. 1. Comparison between Wilson loop computed along principal axis $W_x(k_y)$, also known as Wannier charge centers (WCCs), and the in-plane Wilson loop procedure presented in this work for spinful, time-reversal invariant ($\mathcal{T}$), crystalline insulators, $W_{ABCD}(k_0)$. These procedures are generally nonequivalent in diagnosing band topology in the absence of enhanced symmetry.

pinned at ± 1. Nevertheless, it has been shown that the gap in the spectra of PSO (spin-gap) closes adiabatically. The resulting spin-Chern number, computed using the nondegenerate eigenstates of the PSO, is thus protected by both the spin-gap and bulk energetic gap.

Despite the conceptual power and scope of this method, it faces significant challenges in application to realistic models. Namely, $\hat{s}$ need not correspond to a principal spin quantization axis, it can correspond to an arbitrary (pseudo)spin axis. As a result, the number of possible forms for $\hat{s}$ grows rapidly with an increasing number of bands. Selection of proper $\hat{s}$ is thus extremely challenging without detailed knowledge of the basis or a computationally intensive trial and error procedure.

In this work, we build off a number of landmark studies into the study of the non-Abelian Stokes theorem and its computation using Wilson loops (WLs), going back over fifty years [13–15]. We demonstrate that in crystalline systems, in-plane Wilson loops offer a route to quantifying non-Abelian Berry flux and establish conditions for its quantization in individual Kramers pairs. While WLs are already widely used in diagnosis of band topology through analysis of the non-Abelian Berry phase [16–25], we place special emphasis on understanding the corresponding non-Abelian flux in any n-fold rotationally symmetric plane. Care is taken to ensure that this analysis is agnostic to the choice of basis. Finally, this method is shown to be applicable in both tight-binding models and *ab initio* data.

II. FORMALISM OF IN-PLANE WILSON LOOP

Consider a closed, nonintersecting path lying in the xy plane and respecting the m-fold symmetry of the plane, such as that shown in the right panel of Fig. 1. The WL of SU(2) connections of nth Kramers-degenerate bands along this contour, parameterized by $\boldsymbol{k}(l)$, is defined as

$$W_n = P\exp\left[i\oint\sum_{j=1}^{2} A_{j,n}(\boldsymbol{k}(l))\,\frac{dk_j}{dl}\,dl\right], \tag{1}$$

$$= \exp[i\,\theta_n(k_0)\,\hat{\boldsymbol{\Omega}}_n(k_0)\cdot\boldsymbol{\sigma}], \tag{2}$$

where P denotes path ordering and k_0 corresponds to the edge size of the loop. The intraband connections of nth band, are defined according to the formula $A_{j,n,s,s'}(\boldsymbol{k}) = -i\psi^{\dagger}_{n,s}(\boldsymbol{k})\partial_j\psi_{n,s'}(\boldsymbol{k})$, where $\psi_{n,s}(\boldsymbol{k})$ are the eigenfunctions of nth band, with $s = \pm 1$ denoting the Kramers index, and $\partial_j = \frac{\partial}{\partial k_j}$. It is this Kramers degeneracy which causes the Berry connection to take the form of an SU(2) matrix, making the subsequent computation non-Abelian despite considering only a single Kramers degenerate band. Similar implementations of the Wilson loop have been utilized in Refs. [23–26]. While we will focus on the generic case of an SU(2) Berry connection defined for a single Kramers pair, this formalism can be naturally extended for an arbitrary set of degenerate bands. An example of the Berry connection for fourfold degenerate bands is available in Ref. [27].

The gauge invariant angle $\theta_n(k_0)$ can be related to the magnitude of non-Abelian, Berry's flux by employing a non-Abelian generalization of Stokes's theorem [15,28–31]. The gauge dependent, three-component, unit vector $\hat{\boldsymbol{\Omega}}_n(k_0)$ defining the orientations in SU(2) color space will not be used for computing any physical properties. In the subsequent section, we demonstrate that in the presence of independent $\mathcal{P}$ and $\mathcal{T}$ symmetry, regardless of the existence of a U(1) conservation law, the nth Kramers-degenerate bands support quantized flux of magnitude $|2M\pi|$ with $M \in \mathbb{Z}$, $|\Delta\theta_n(k_0)| = |\theta_n(k_0) - \theta_n(0)|$ will interpolate from 0 to $|2M\pi|$ as k_0 is systematically increased from 0 to a final value k_f, when the area enclosed by the loop becomes equal to the area of two-dimensional BZ. In other cases, such as generic two-dimensional insulators which break $\mathcal{P}$ symmetries, this method remains viable in special cases which will be discussed further in the following section.

The current standard for topological analysis of *ab initio* data, involves calculation of Wannier charge centers (WCCs). WCCs are so-called because a direct correspondence can be made with the real-space expectation value of the Bloch wavefunction. Such a correspondence arises due to the path of integration coinciding with a single cycle of the Brillouin zone, invoking the periodicity of the Brillouin zone. A schematic of this computation is visible on the left side of Fig. 1. The computation of WCCs and analysis of the resulting spectra when computed as a function of a transverse momenta have emerged as powerful tools for describing topology of quasi-particle band structures [16–19].

Generally WCCs are used for diagnosis of the Fu-Kane strong and weak Z_2 indices. In the presence of mirror-symmetry or nondegenerate bands, they are further utilized to determine quantized Berry's flux [21]. However, in the absence of a U(1) conservation law WCCs fail to recognize flux in spinful band structures. This is due in part to the fact that computation of WCCs discretizes the Brillouin zone into a series of one-dimensional insulators for which the one-dimensional winding number is computed.

For topological insulators supporting gapless surface states, the WCC spectra displays a spectral flow. This flow is utilized to establish the bulk-boundary correspondence. It is thus natural that this analysis of WCCs fails to identify nontrivial topology for the class of higher-order topological insulators (HOTIs) for which gapless surface states are absent. In these situations, performing the WL along a closed contour in the plane, ensures that the two-dimensional bulk invariant

is probed rather than inferred through an analysis of a series of one-dimensional insulators.

We will explicitly demonstrate the power of the in-plane Wilson loop by performing topological classification of continuum, lattice, and *ab initio* band structures of Dirac semimetals (DSMs). We choose to examine DSMs as the generic two-dimensional planes lying between the Dirac nodes and perpendicular to the axis of nodal separation have been identified as examples of two-dimensional higher-order topological insulators with gapped edge states, while the high-symmetry planes are identified by either a Z_2 index, or a mirror Chern number, depending on the presence of mirror symmetry [32–36]. DSMs thus offer the chance to study distinct types of higher order and first-order topological insulators, embedded in a single material.

III. MODEL AND SYMMETRIES

Na_3Bi was proposed as the first candidate material for realizing stable DSMs, which arise from linear touching between a pair of twofold, Kramers-degenerate bands at isolated points of momentum space, along an axis of n-fold rotation (say the $\hat{z}$ or c axis) [37–39]. The Dirac points are simultaneously protected by the combination of parity and time-reversal symmetries ($\mathcal{PT}$) and the n-fold rotational ($\mathcal{C}_n$) symmetry [40,41]. The low energy Hamiltonian is written as, $H(\boldsymbol{k}) = \epsilon_0(\boldsymbol{k})\mathbb{1} + \sum_{j=1}^{5} d_j(\boldsymbol{k})\Gamma_j$, where Γ_j's are again five, mutually anti-commuting, 4×4 matrices, and $\mathbb{1}$ is the 4×4 identity matrix [37]. The topological properties of conduction and valence bands are controlled by the $O(5)$ vector field $d_1 = Ak_x$, $d_2 = Ak_y$, $d_3 = Bk_z(k_x^2 - k_y^2)$, $d_4 = 2Bk_xk_yk_z$, and $d_5 = M_0 - M_1k_z^2 - M_2(k_x^2 + k_y^2)$, where A, B, M_0, M_1, and M_2 are band parameters. For Na_3Bi, the parameters $M_0 < 0$, $M_1 < 0$, and $M_2 < 0$ capture band inversion effects, leading to two Dirac points along the sixfold, screw axis at $(0, 0, \pm k_D)$, with $k_D = \sqrt{M_0/M_1}$. The particle-hole anisotropy term $\epsilon_0(\boldsymbol{k})$ does not affect band topology.

For describing low-energy physics of massless Dirac fermions, d_3 and d_4 terms can be ignored in the renormalization group sense [37,42,43]. Such approximate theories predict topologically protected, loci of zero-energy surface states, also known as the *helical Fermi arcs*, joining the projections of bulk Dirac points on the (100) and the (010) surface-Brillouin zones. Therefore the spectroscopic detection of *helical Fermi arcs* was often considered to be the smoking gun evidence of bulk topology of DSMs. However, these terms cannot be ignored for addressing topological properties of generic planes and they are responsible for gapping out the helical edge states for all $|k_z| < k_D$ and $k_z \neq 0$ [38,44,45], and giving rise to higher-order topology [34,46].

A. Bulk topology of continuum models

Here we provide proof of the correspondence between in-plane Wilson loop and quantized non-Abelian flux for a continuum model of the two-dimensional planes embedded in a Dirac semimetal, perpendicular to the direction of nodal separation. We omit third-order terms such that all WLs are analytically tractable with the model taking the form

$$H(\mathbf{k}) = \sin\alpha(k_\perp)\cos(m\phi)\Gamma_1 + \sin\alpha(k_\perp)\sin(m\phi)\Gamma_2 + \cos\alpha(k_\perp)\Gamma_3, \tag{3}$$

fixing $\Gamma_{i=1,2,3} = \tau_i \otimes \sigma_1$, $\Gamma_4 = \tau_2 \otimes \sigma_0$, $\Gamma_5 = \tau_3 \otimes \sigma_0$, where τ_0 and σ_0 are two 2×2 identity matrices. The two sets of Pauli matrices τ_j and σ_j with $j = 1, 2, 3$ operate on the spin and orbital degrees of freedom respectively. We further define $\cos\alpha(k_\perp) = (\Lambda - k_\perp^{2m})/(\Lambda + k_\perp^{2m})$, with Λ defining the skyrmion core size. Typically, this model is written in a block diagonal basis such that a U(1) Abelian Berry connection can be written for the occupied eigenstate of each block. When $\mathrm{sgn}(\Lambda) > (<)0$, it is then straightforward to show that the model is topological (trivial) as the Abelian Berry curvature computed using the U(1) Berry connection displays quantized $|2m\pi|$ (0) Berry's flux [6].

In the current basis, the model is block off-diagonal, and the SU(2) intraband Berry's connections are matrix valued, i.e., non-Abelian. Following the procedure described in Sec. II, identification of quantized flux relies on tracking interpolation of the in-plane Wilson loop between SU(2) center elements $\pm\sigma_0$ as the area enclosed by the loop is systematically increased until commensurate with the Brillouin zone boundary. A continuous interpolation between these elements is taken to be in correspondence with the interpolation of the non-Abelian flux, $\theta_{c/v}$, by 2π as $\mathrm{Tr}W_{xy} = 2\cos\theta_{c/v}$. To prove that the non-Abelian in-plane Wilson loop precisely measures flux, we consider a path enclosing a sector of the circular Brillouin zone with central angle $2\pi/N$. The non-Abelian WL can thus be written as

$$W_N = W^{k_\perp=\infty}_{k_\perp,k_\perp=0}(\phi = \phi_i)W^{\phi_i+2\pi/N}_{\phi,\phi_i}(k_{\perp=\infty}), \quad W^{k_\perp=0}_{k_\perp,k_\perp=\infty}(\phi = \phi_i + 2\pi/N). \tag{4}$$

After some algebra, using the definition for the intraband Berry's connections,

$$A_j(\boldsymbol{k}) = \frac{1}{2|\boldsymbol{N}|(|\boldsymbol{N}| + N_5)}\Big[(N_1\partial_j N_2 - N_2\partial_j N_1)\Gamma_{12} + (N_2\partial_j N_3 - N_3\partial_j N_2)\Gamma_{23} + (N_3\partial_j N_1 - N_1\partial_j N_3)\Gamma_{31} + \sum_{a=1}^{3}(N_a\partial_j N_4 - N_4\partial_j N_a)\Gamma_{a4}\Big], \tag{5}$$

where $\Gamma_{ij} = [\Gamma_i, \Gamma_j]/(2i)$, we arrive at the form

$$\tfrac{1}{2}Tr[W_N] = \cos^2\Omega + \cos(2m\pi/N)\sin^2\Omega, \tag{6}$$

where

$$\Omega = \begin{cases} \pi/2, & \mathrm{sgn}(\Lambda) > 0 \\ 0, & \mathrm{sgn}(\Lambda) < 0 \end{cases}. \tag{7}$$

We can conclude that in the topological phase, $\mathrm{sgn}(\Lambda) > 0$ and $\mathrm{Tr}W_N/2 = \cos(2m\pi/N)$. As such we have directly shown correspondence between quantized Berry's flux, $\theta_{c/v}$ and the in-plane Wilson loop, validating the above procedure of tracking SU(2) center elements.

Additionally, we could consider analyzing $W_\phi(\mathbf{k}_\perp)$ as a function of $k_\perp$. After some algebra, we arrive at the

expression,

$$\mathrm{Tr}W_\phi(\mathbf{k}_\perp)/2 = \cos(m\pi)\cos(m\pi\sqrt{10-6\cos(2\alpha)}/2). \quad (8)$$

We note that in the simple case, $m = 1$, $\mathrm{Tr}W_\phi(\mathbf{k}_\perp *)/2 = -1$ where $k_\perp{*}^{2m} = \Lambda$ is the curve defining band inversion. However, such correspondence vanishes for $m > 1$, as $W_\phi(\mathbf{k}_\perp) = \pm\sigma_0$ at general values of $k_\perp$, which are not in correspondence with the location of band inversion.

Having proven the capability of the in-plane Wilson loop to detect non-Abelian Berry flux, let us now consider the consequences of reintroducing higher-order terms into the continuum model such that it takes the form of a five component vector,

$$\hat{H}(\boldsymbol{k}) = \sum_{j=1}^{5} N_j(\boldsymbol{k})\Gamma_j = B_1 k_\perp(\cos\phi\Gamma_1 + \sin\phi\Gamma_2) + B_2(k_z)k_\perp^2(\cos 2\phi\Gamma_3 + \sin 2\phi\Gamma_4) + N_5(k_\perp, k_z)\Gamma_5, \quad (9)$$

where $(k_x, k_y) = k_\perp(\cos\phi, \sin\phi)$. At this step we emphasize that $N_5(k_\perp, k_z)$ is defined such that for $k_\perp = 0(\infty)$, $|k_z| < k_D$, $N_5/\mathbf{N} = -(+)1$ while for $k_\perp = 0(\infty)$, $|k_z| > k_D$, $N_5/\mathbf{N} = +(+)1$. This definition is important as it makes definitive the presence of band inversion between the high-symmetry locations $k_\perp = 0$ and $k_\perp = \infty$ for all $|k_z| < k_D$, which can be observed through a sign change in symmetry eigenvalues of $\mathcal{P} = \Gamma_5$ for the occupied eigenstates at these locations.

The non-Abelian Berry connection, A_ϕ, can then be calculated using Eq. (5). The in-plane Wilson loop taking the form

$$W_\phi^\pm(k_\perp, k_z) = \mathcal{P}\exp\left[i\int_0^{2\pi} A_\phi(\mathbf{k})d_\phi\right], \quad (10)$$

where $(\pm)$ indicates the Kramers degenerate conduction and valence bands respectively. Defining $W_\phi^\pm(k_\perp, k_z) = \exp(i\Phi^\pm \cdot \sigma)$, we examine the gauge invariant quantity $\cos\Phi^\pm = -\cos\alpha^\pm$. This quantity is equivalent to $\mathrm{Tr}(W_\phi^\pm)/2$. Solving for $\alpha^\pm$, we arrive at the form

$$\alpha^\pm = \pi\left[\left(\frac{(B_1^2 \pm 2B_2(k_z)^2k_\perp^2)k_\perp^2}{\mathbf{N}(\mathbf{N}+N_5)} - 1 \mp 2\right)^2 + \frac{B_1^2B_2(k_z)^2k_\perp^6}{\mathbf{N}^2(\mathbf{N}+N_5)^2}\right]^{\frac{1}{2}}. \quad (11)$$

We will now investigate this quantity in three important limits (1) at the nodal plane, (2) at the mirror plane, and (3) at a generic plane.

Nodal plane. At the nodal plane, $|k_z| = k_D$, as $k_\perp \to 0$, $\mathbf{N}$ scales as $k_\perp$. As a result $\alpha^\pm(k_{\perp\to 0}) = 2\pi$ while in the limit $k_\perp \to \infty$, $\alpha^\pm(k_{\perp\to\infty}) = \pi|-1\mp 2|$. We therefore find the quantized flux in the nodal plane to be $|\Delta\Phi| = |\Phi(k_\perp = \infty) - \Phi(k_\perp = 0)| = \pi$, the critical value. We emphasize that extraction of this critical value is an advantage of the in-plane Wilson loop as the spin-Resolved Wilson loop can no longer be applied in this plane [11,12].

Mirror plane. For the current model, $B_2(k_z) = k_zB_2$, therefore at the mirror plane, $k_z = 0$, we set $B_2(k_z) = 0$. In order for a plane to support quantized non-Abelian flux of magnitude 2π, we must be able to show that $\mathrm{Tr}W_\phi^\pm$ evolves adiabatically from $+2 \to +2$, through $\mathrm{Tr}W_\phi^\pm = -2$. We note $\alpha^\pm(k_{\perp\to 0,\infty}) = \pi|-1\mp 2|$, while the values of $k_\perp$ for which $\mathrm{Tr}W_\phi^\pm = -2$ are identified in the mirror plane by solving

$$\left|\frac{B_1^2k_\perp^2}{\mathbf{N}(\mathbf{N}+N_5)} - 1 \mp 2\right| = 2n, n \in \mathcal{N}. \quad (12)$$

This equation satisfied if there exists a value of $k_\perp$ for which $N_5 = 0$. Given the criteria for N_5 at $k_\perp = 0$ and $k_\perp = \infty$, this must be satisfied for $k_z = 0$. We can therefore conclude that the mirror plane supports quantized non-Abelian flux of magnitude 2π.

Generic plane. At a generic value of k_z, we can again conclude that $\alpha^\pm(k_{\perp\to 0,\infty}) = \pi|-1\mp 2|$, however we can no longer analytically determine how $\alpha^\pm$ interpolates between these values. We thus solve numerically, fixing $B_2(k_z) = k_zB_2$ and $N_5 = (B_3k_\perp^4 + B_4k_z^2 - \Delta)$. Carrying out this computation, we determine that all planes for which $|k_z| < k_D$ support quantized non-Abelian flux of magnitude 2π.

At this point, we emphasize the importance of how N_5 is defined. Specifically, this function is defined such that a Wilson line along the boundary of the Brillouin zone yields a quantized result, $\mathrm{Tr}W_\phi^\pm(k_\perp \to \infty) = \cos(N\pi)$ with $N \in \mathbb{Z}$. This is the only condition which we impose and it is trivially satisfied in two-dimensional systems supporting inversion symmetry. As a result we can conclude that quantized non-Abelian flux can be computed using the method of in-plane Wilson loops for individual bands of spinful two-dimensional insulators supporting $\mathcal{P}$ regardless of the presence of a U(1) conservation law. We now consider implementation of the in-plane Wilson loop in lattice tight-binding models.

IV. MINIMAL TIGHT-BINDING MODELS

We consider a lattice regularization of Eq. (9). The Bloch Hamiltonian takes the form $H(\mathbf{k})_n = \sum_{j=1}^5 N_j^n(\mathbf{k})\Gamma_j$, where

$$\mathbf{N}(\mathbf{k})^n = \{t_p\sin k_x, t_p\sin k_y, t_d\lambda_1(\mathbf{k}), t_d\lambda_2(\mathbf{k}), t_s(2-\cos k_x - \cos k_y - \cos k_z)\}. \quad (13)$$

The lattice constants have been set to unity, t_j's are hopping parameters with units of energy and the Dirac points are located at $(0, 0, \pm k_D)$, where $k_D = \pi/2$. In general, $\lambda_n(k_\perp)$ represent further neighbor hopping terms allowed by C_{4z} symmetry and which preserve the inversion symmetry generated by $\mathcal{P} = \Gamma_5$, such that $\mathcal{P}^\dagger H(\mathbf{k})\mathcal{P} = H(-\mathbf{k})$.

At this point, we emphasize the additional constraint expressed in the previous section, namely that inversion symmetry be further preserved within the xy plane parameterized by k_z which comprises a two-dimensional insulator embedded in the three-dimensional system. To enforce this condition, we select $\lambda_1(k_\perp) = \sin k_x\cos k_y$ and $\lambda_2(k_\perp) = \sin k_y\cos k_x$, such that within a generic plane defined by $k_z \neq 0$, $\mathcal{P}^\dagger H(k_x, k_y)\mathcal{P} = H(-k_x, -k_y)$. Fourfold rotational symmetry about the z-axis is preserved, generated by $C_{4z}^\dagger H(\mathbf{k})C_{4z} = H(\mathbf{k}')$, where $C_{4z} = e^{i\frac{3\pi}{4}\tau_0\otimes\sigma_3}e^{i\frac{3\pi}{4}\tau_3\otimes\sigma_3}$ and $\mathbf{k}' = \{k_y, -k_x\}$. Having fixed the conditions protecting the presence of quantized non-Abelian flux, we examine its computation for $|k_z| < k_D$ and $|k_z| > k_D$. The distinct topology of the the planes is then establish by computing the in-plane WL. It is

convenient to compute WL by following a $\mathcal{C}_4$ symmetric path, denoted *ABCD* as seen in Fig. 1. Without any loss of generality we will choose the point A with $(k_x, k_y) = (-k_0, -k_0)$ as our reference point. When the Kramers-degenerate wave functions are parallel transported between an initial point $\boldsymbol{k}_i$ and a final point $\boldsymbol{k}_f$, the matrix-valued, non-Abelian Berry's phase. [13–15,29,47,48] is described by the Wilson line (or non-Abelian holonomy)

$$W_{i,f} = P \exp\left[i \int_{l_i}^{l_f} \sum_{j=1}^{2} a_j(\boldsymbol{k}(l)) \frac{dk_j}{dl}\, dl \right], \tag{14}$$

where P denotes path ordering, and we choose to work with the gauge choice given in Eq. (5). We note that $A_j(\boldsymbol{k})$ is singular at TRIM locations in which $N_5 = -|\boldsymbol{N}|$ as discussed in Tyner *et al.* [31]. We have parameterized the line, joining two points as $k_j(l)$, $\boldsymbol{k}_i = \boldsymbol{k}(l_i)$ and $\boldsymbol{k}_f = \boldsymbol{k}(l_f)$. Therefore the WL for path *ABCD* can be obtained as the ordered product of four straight Wilson lines as

$$W_{ABCD}(k_0) = W_{A,B} W_{B,C} W_{C,D} W_{D,A}. \tag{15}$$

Since $W_{ABCD}(k_0) \in Spin(4)$, we can parametrize it as

$$\begin{aligned} W_{ABCD}(k_0) &= W_{ABCD,c}(k_0) W_{ABCD,v}(k_0) \\ &= \begin{bmatrix} \exp[i\theta_c(k_0)\, \hat{\boldsymbol{n}}_{cj}(k_0) \cdot \boldsymbol{\sigma}] & 0 \\ 0 & \exp[i\theta_v(k_0)\, \hat{\boldsymbol{n}}_v(k_0) \cdot \boldsymbol{\sigma}] \end{bmatrix}. \end{aligned} \tag{16}$$

Here, $W_{ABCD,c}(k_0) \in \mathrm{SU}(2)$ and $W_{ABCD,v}(k_0) \in \mathrm{SU}(2)$ are the WLs for the respective SU(2) connections of conduction and valence bands. Two angles $\theta_c(k_0)$ and $\theta_v(k_0)$ are gauge-invariant and two $O(3)$ unit vectors $\hat{\boldsymbol{n}}_c(k_0)$ and $\hat{\boldsymbol{n}}_v(k_0)$ define gauge-dependent orientations in color space.

If we wish to abstain from making a gauge choice and compute WLs in a purely numerical fashion, the straight Wilson line along $\hat{j}$ for band n can be rewritten as [16,19,32],

$$W_j(\mathbf{k}) = F_{j,\mathbf{k}+N_j\Delta k_j} \ldots F_{j,\mathbf{k}+\Delta k_j} F_{j,\mathbf{k}}, \tag{17}$$

where $F_{j,\mathbf{k}+N_j\Delta k_j} = \langle u^n_{\mathbf{k}+\Delta k_j} | \, | u^n_{\mathbf{k}} \rangle$, $\Delta k_j = 2\pi/N_j$, and $|u^n_{\mathbf{k}}\rangle$ is the Bloch function of band n at $\mathbf{k}$.

From $\theta_{c/v}(k_0)$ we can construct other gauge-invariant quantities, such as the eigenvalues of WLs $\exp[\pm i\theta_{c/v}(k_0)]$, the trace of WLs $\mathrm{Tr}[W_{ABCD,c/v}](k_0) = 2\cos[\theta_{c/v}(k_0)]$, and the Vandermonde determinant $D_V[W_{ABCD,c/v}](k_0) = 2i \sin[\theta_{c/v}(k_0)]$. In gauge theory literature, $\mathrm{Tr}[W_C]$ is the most widely studied observable. It is useful for detecting interpolation of W_C between the center elements $\pm\sigma_0$ of SU(2) group, leading to $\mathrm{Tr}[W_C] = \pm 2$. When $\theta_{c,v} = 2l\pi$ $[(2l+1)\pi)]$, with $l \in \mathbb{Z}$, $W_{C,c/v} = \sigma_0$ $[-\sigma_0]$. We determine both $\mathrm{Tr}[W_{ABCD,c/v}]$ and $D_V[W_{ABCD,c/v}]$ to find $\theta_{c/v}$. The results are then shown in Fig. 2(a). It is clear that the $|k_z| < k_D$ plane supports Berry's flux which quantizes to a value of $|2\pi|$.

A. Distinction from principal axis Wilson loop

At this point it is sensible to argue that although a mirror Chern number can not be defined for Eq. (13), the bulk topology of the plane can be determined via the two-dimensional Fu-Kane $\mathbb{Z}_2$ index. Here we provide an example in which the in-plane Wilson loop is able to capture nontrivial topology invisible to the Fu-Kane index, or computation of WCCs. In constructing this model we take advantage of the property stated in the previous section, that we require the Wilson line along the boundary of the Brillouin zone to be quantized. While this is satisfied for systems supporting inversion symmetry, it is also possible to relax the requirement of inversion symmetry throughout the two dimensional Brillouin zone, imposing this condition only at the Brillouin zone boundary. As an example consider alteration of Eq. (13) to the form,

$$\begin{aligned} \mathbf{N}(\mathbf{k}) = \{ & t_p \sin k_x \cos k_y,\, t_p \sin k_y \cos k_x, \\ & t_d \sin k_x \sin k_y,\, 0,\, t_s(1 - \cos k_x \cos k_y - \cos k_z) \}. \end{aligned} \tag{18}$$

In this form, the location of the Dirac nodes along the k_z axis are unaltered as well as the generator inversion symmetry $\mathcal{P}$. The generator of C_{4z} is altered to the form, $C_{4z} = e^{i\frac{3\pi}{4}\tau_0\otimes\sigma_3} e^{i\frac{\pi}{2}\tau_3\otimes\sigma_3}$. However, if we consider a generic two-dimensional plane parameterized by k_z, $\mathcal{P}^\dagger H(k_x, k_y)\mathcal{P} \neq H(-k_x, -k_y)$. Nevertheless, inspecting the Brillouin zone boundary, $(k_x = \pm\pi, k_y)$ or $(k_x, k_y = \pm\pi)$, this relation is restored. We can thus compute the value of quantized non-Abelian flux in a generic xy plane. The results of the in-plane Wilson loop computed for $|k_z| < k_D$ and $|k_z| > k_D$ are shown in Fig. 2(b). These results are consistent with the prior analysis and demonstrate nontrivial topology supported by planes parameterized by $|k_z| < k_D$. In correspondence, we note the presence of surface bound modes for these planes in Fig. 2(c). We then contrast this method with computation of the WCC spectra in Fig. 2(d), demonstrating that the WCC spectra yields trivial results for both planes, establishing the two techniques as distinct. For an example of the use of this method in a higher-order insulator supporting corner bound modes please consult the supplementary material [49].

For an additional example of a realistic band structure in which the WCC spectra and in-plane Wilson loop return topologically distinct results, please refer to Ref. [50]. The method of in-plane Wilson loop is utilized in tandem with the spin-resolved technique developed by Prodan [11], to confirm the existence of an even-integer spin Chern number in Kramers degenerate bands of β-bismuthene which have been labeled trivial via analysis of WCCs. Given the capability of existing software packages such as Z2Pack [21] to efficiently compute Wilson loops in *ab initio* data, we now consider application of this formalism to *ab initio* models of DSMs.

V. *AB INITIO* BAND STRUCTURES

The crystal structure of Na_3Bi, belongs to the space group $P6_3/mmc$ and has the lattice constants $a = b = 5.49$ Å,

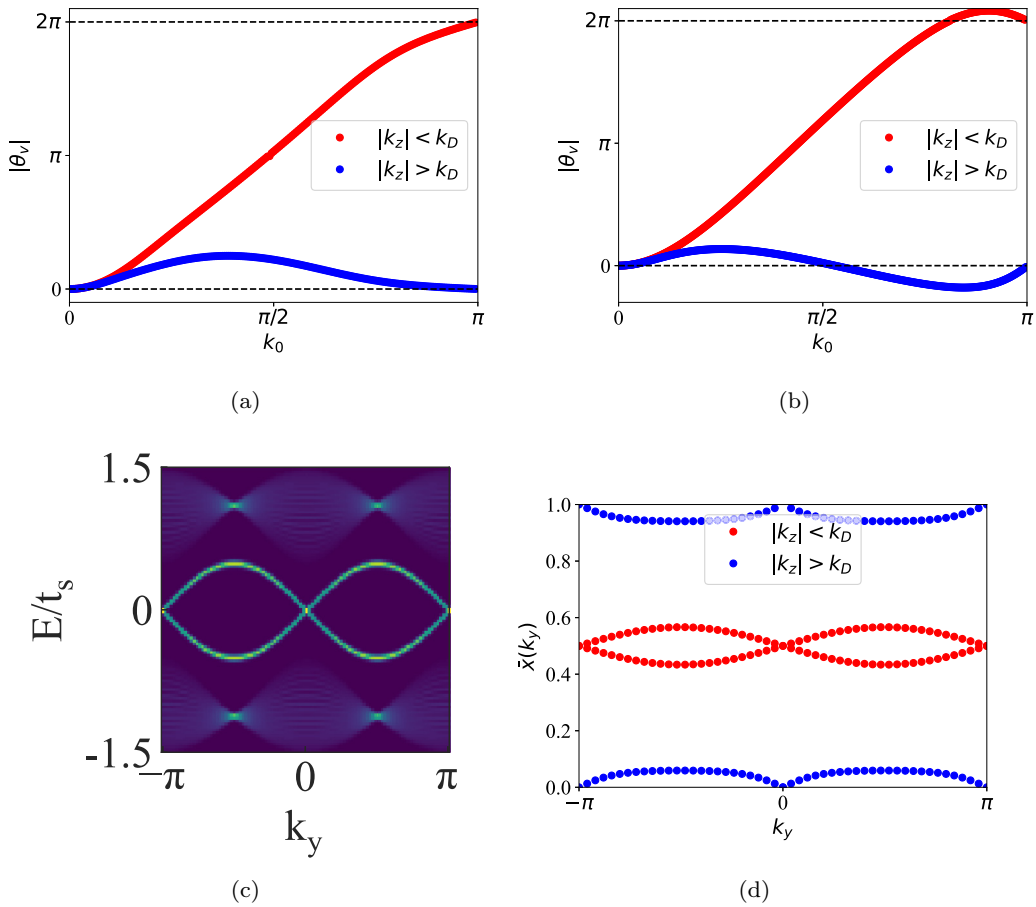

FIG. 2. (a) Results of in-plane Wilson loop following a C_4 symmetric closed contour for the model given in Eq. (13). As the area enclosed by the contour approaches the area of the Brillouin zone ($k_0 = \pi$), the flux converges to $|2\pi|$. (b) Results of in-plane Wilson loop following a C_4 symmetric closed contour for model given in Eq. (18) demonstrating quantized non-Abelian flux of magnitude $|2\pi|$. (c) Spectral density on (10) edge for tight-binding model given by Eq. (18) for $|k_z| < k_D$. All calculation are performed fixing $t_p = t_p = t_s = t_d = 1$. (d) Wannier center charge spectra, $\bar{x}(k_y)$, for identical choice of hopping parameters in Eq. (18). In contrast to the in-plane Wilson loop, the WCC spectra does not display winding and thus cannot detect the nontrivial band topology of the system.

$c = 9.78$ Å. It consists of two nonequivalent Na sites, denoted by Na(1) and Na(2). The honeycomb layers formed by Na(1) and Bi are stacked along the c axis, with Na(2) sites located between the layers [51–63]. For computational details please see the supplementary material [49] (see also Refs. [64–66] therein). The calculated band structures within the energy window -3 and $+2$ eV are displayed in Fig. 3(a). We have labeled the Kramers-degenerate bands, according to their energy eigenvalues at the Γ point, with $E_n(0) < E_{n+1}(0)$. The bulk Dirac points arise from linear touching between bands $n = 6$ and $n = 7$, along the sixfold, screw axis (A-Γ-A line or the k_z axis) at $(0, 0, \pm k_D)$, with $k_D \approx \pm 0.29 \times \frac{\pi}{c}$. Their reference energy coincides with the Fermi level.

A. Bulk topology

In order to perform topological analysis of various bands, we have employed maximally localized Wannier functions calculated using the WANNIER90 package [67]. We will calculate WLs of individual SU(2) Berry's connections of bands $n = 1$ through $n = 6$ by utilizing the Z2Pack software package [18,21]. In calculating in-plane WLs, we have followed the hexagonal path $abcdef$, shown in Fig. 3(b). This is efficiently accomplished utilizing the existing Z2Pack functions through definition of a custom path for integration, $f(t_1, t_2)$, where $t_j \in [0, 1]$; t_2 parametrizing the hexagonal path and t_2 parametrizing the area enclosed by the contour.

We first focus on the results of the in-plane Wilson loop for occupied bands in the $k_z = 0$ mirror plane. In this plane, we find that the Dirac band ($n = 6$) as well as four remote bands ($n = 1, 2, 3, 5$) support nonzero flux of varying magnitude [see Fig. 3(c)] for which quantization occurs for a contour exactly enclosing the two-dimensional BZ. Due to the presence of mirror symmetry, flux could also have been computed via WCCs, yielding identical results. As we adiabatically tune k_z away from the mirror plane, WCCs can no longer be utilized to determine flux. For more details of WCCs in these planes please see the Supplementary Material [49]. Computing WLs for the occupied Dirac band at generic planes defined by $|k_z| < k_D$, $|\Delta\theta_6(k_0)|$ does not display 0 to 2π interpolation within the Brillouin zone. In the continuum model of Eq. (9), such a situation would be encountered by fixing $N_5/\mathbf{N} = +1$ at $k_\perp = 0$, $|k_z| < k_D$ and $-1 < N_5/\mathbf{N} < 0$ at $k_\perp = \infty$, $|k_z| < k_D$. Nevertheless, we observe deviation from quantization within the Brillouin zone occurs adiabatically. These topological properties of Dirac bands are identical to

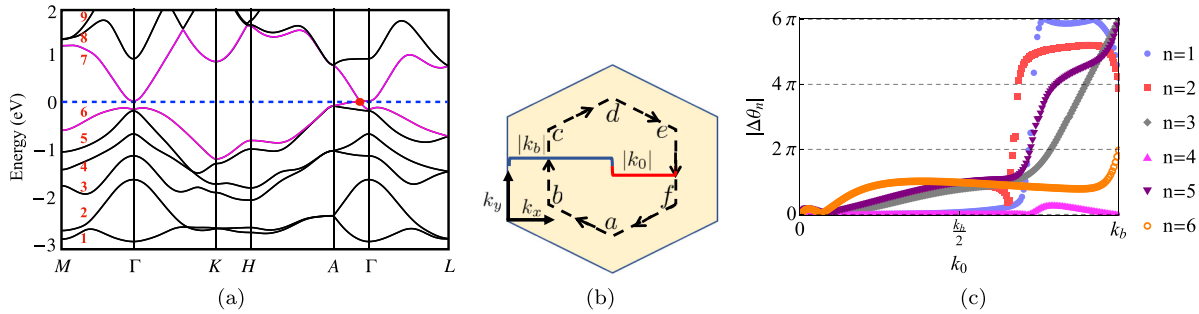

FIG. 3. (a) The *ab initio* band structures of Na_3Bi are plotted along various high- symmetry directions, and the Kramers-degenerate bands are labeled, following an ascending order of energy eigenvalues at the Γ point. The linear touching between bands $n = 6$ and 7 (purple colored), along the sixfold, screw axis Γ-A, gives rise to bulk Dirac points (red dot), lying at the Fermi level (dashed line). (b) The Wilson loops are calculated following the hexagonal loop *abcdef*. We increase k_0 from zero to $k_b = \pi/a$, when the enclosed area becomes equal to that of hexagonal Brillouin zone (yellow). The gauge invariant eigenvalues of Wilson loops are given by $e^{\pm i\theta_n(k_0)}$, where n is the band index. For topologically nontrivial bands, supporting non-Abelian flux of magnitude $2M\pi$, $|\Delta\theta_n| = |\theta_n(k_0) - \theta_n(0)|$ will interpolate from 0 to $2M\pi$, as k_0 is increased from 0 to k_b. (c) At the $k_z = 0$ plane, the bands $n = 1, 2$ ($n = 3, 5$) support quantized flux of magnitude $4\pi\,(6\pi)$ and band $n = 6$ supports flux of magnitude 2π.

what have been found from the effective, four-band model of sp-hybridized DSMs [31].

While topological diagnosis of the high-symmetry planes of Na_3Bi benefits from the presence of mirror symmetry, one can also consider a DSM where the high-symmetry plane lying perpendicular to the direction of nodal separation lacks mirror symmetry. One such system is β-CuI, which was proposed as a DSM by Le *et al.* [38], with the Dirac nodes lying along the k_z axis. For full computational details of this material please consult the supplementary material [49]. As β-CuI belongs to space group $R\bar{3}m$, the high-symmetry xy planes support threefold rotational symmetry. Mirror symmetry is therefore absent and the current topological classification of the planes is limited to assignment of a Z_2 index. In Fig. 4(b), we show that for the high-symmetry plane lying between the Dirac nodes, the method of in-plane WLs can be utilized to identify a quantized flux. Furthermore, at a generic plane lying between the Dirac nodes the adiabatic deviation of the in-plane loop from the quantized result provides evidence of higher-order topology.

VI. BULK-BOUNDARY CORRESPONDENCE

Recently, Tyner *et al.* [31] demonstrated that unlike Weyl semimetals, the surfaces of Dirac semimetals do not support loci of two, degenerate zero energy state beginning and terminating at the projection of the bulk nodes [31]. Rather, a generic plane lying between the Dirac nodes supports two, nondegenerate gapped surface states. Only at the high-symmetry mirror planes can we locate gapless points on the surface with the number of gapless points being determined by the magnitude of the mirror Chern number. Using the iterative Green's function method [68] and the WANNIER TOOLS software package [69], we plot the spectral density on the (100) surface of Na_3Bi in Fig. 5. These results verify that at a generic value of $|k_z| < k_D$, the (100) surface of Na_3Bi supports gapped surface states. Only at the $k_z = 0$ mirror plane do we find a gapless state in correspondence with the admission of mirror Chern number $|\mathcal{C}_m| = 1$, by this plane.

In recent works, the bulk-boundary correspondence of two dimensional higher order insulators has been characterized

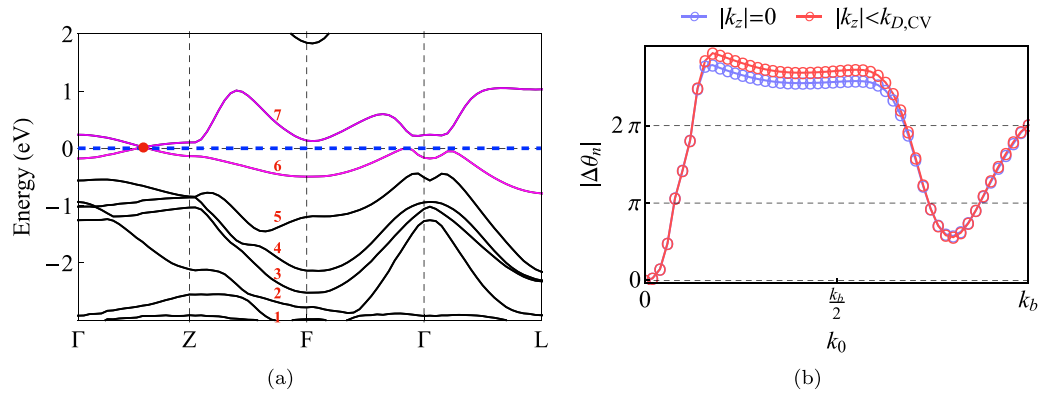

FIG. 4. (a) Band structure of β-CuI in the primitive unit cell along high symmetry path detailed by Le *et al.* [38]. Kramers pairs which touch at the Fermi energy at $\mathbf{k} = (0, 0, \pm k_D)$ to produce Dirac point (bands in Dirac subspace) are colored purple. Dirac point is noted with red dot. (b) Results of Wilson loop calculation at high-symmetry plane, $k_z = 0$, and generic value of $|k_z| < k_{D,CV}$, where $k_{D,CV}$ is the location of the Dirac point in the conventional unit cell for the occupied Dirac band, $n = 6$. Wilson loop is calculated as a function of the area enclosed by the Wilson loop path. This calculation indicates that band 6 supports non-Abelian flux of magnitude 2π for $k_z = 0$.

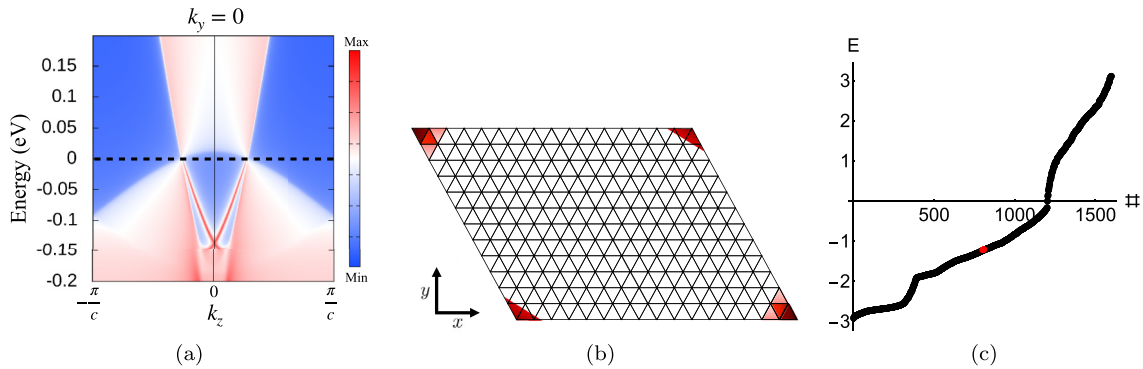

FIG. 5. (a) The (100) edge state dispersion for Na_3Bi along the k_z axis shows the dependence of gap as a function k_z. The normalizability of surface states breaks down at the images of bulk Dirac points on the surface Brillouin zone. (b) Schematic of localization pattern for the four corner-localized states at half-filling in eight band tight binding model of Na_3Bi, setting $|k_z| < |k_D|$ and solving on a finite slab of 10×10 primitive unit cells. Darker shading corresponds to stronger localization. The localization pattern confirms that the xy planes between the Dirac nodes, which have been identified as higher order topological insulators, support corner localized states. (c) States resulting from exact diagonalization calculation. Localization shown in (b) corresponds to states colored in red. We note that while these states exist at half-filling, they do not fall at zero energy and are not separated in energy from the bulk states.

by the presence of corner localized states in those corners of a two-dimensional slab that align with the corners of the primitive two-dimensional unit cell [32–34]. Fixing $|k_z| < k_D$, and performing an exact diagonalization calculation for a slab consisting of 10×10 primitive unit cells in the xy plane, we schematically depict the wavefunction localization of the four corner-localized states present at half filling in Fig. 5(b). The localization pattern of these states captures the bulk-boundary correspondence and verifies the HOTI classification of the xy planes between the Dirac nodes. However, we emphasize that these states are not mid-gap states, well separated from the bulk states [34], posing a significant challenge for experimental detection and re-enforcing the need for a robust method of bulk classification.

VII. CONCLUSION

In summary, we have proposed a method capable of quantifying non-Abelian flux in the two-dimensional Brillouin zone. To place in context the advantages provided by the in-plane Wilson loop it is useful to briefly remark on existing alternative methods. One such alternative is Euler classification, shown to be applicable in two-dimensional spinful insulators supporting $C_2\mathcal{T}$ symmetry [70,71]. However, Euler classification requires identification of a real basis for the Bloch Hamiltonian. While this can be accomplished via Takagi transformation [70], a detailed knowledge of the basis is required. This poses a significant computational challenge for numerical models of real materials, such as those produced by the WANNIER90 software package [67].

Separate procedures for computing the bulk invariant of individual Kramers pairs in the presence or absence of a U(1) conservation law through analysis of the non-Abelian Berry connection guided by the crystalline rotation symmetry are given in Refs. [23–25]. In particular, in Refs. [23,24] a correspondence is drawn between the proposed method and splitting of elementary band representations (EBRs), a core concept of topological quantum chemistry [72–83]. We remark that our work yields identical conclusions to Refs. [23,24] for systems exhibiting split EBRs. However, we have further considered materials "invisible" to topological quantum chemistry methods in Sec. IV A and focused on establishing a direct connection with the presence of an underlying quantized non-Abelian Berry flux.

To summarize, in recent years the topological classification of spinful, two-dimensional insulators has expanded beyond assignment of the Fu-Kane Z_2 index [7] or mirror Chern number, when allowed by symmetry. This is in part due to the increased relevance of nonsymmetry indicative phases such as higher-order insulators [32–34,46]. While the existing methods have been successfully used to diagnose nontrivial topology in such systems, their dependence on explicit knowledge of the basis organization poses a clear obstacle to widespread and efficient implementation. We have introduced and applied the method of in-plane Wilson loops to idealized tight-binding models and *ab initio* data. Our results are insensitive to the number of underlying bands, suggesting the topology of real materials can be addressed with stable, bulk invariants without detailed knowledge of the basis.

ACKNOWLEDGMENTS

A.C.T., S.S., Q.Z., P.D., D.P., J.M.R., and P.G. were supported by the National Science Foundation MRSEC program (DMR-1720139) at the Materials Research Center of Northwestern University. D.P. Simulations made use of the DOD-HPCMP and D.P. Q.Z. and P.D. made use of the Center for Nanoscale Materials (CNM). Work performed at the Center for Nanoscale Materials, a U.S. Department of Energy Office of Science User Facility, was supported by the U.S. DOE, Office of Basic Energy Sciences, under Contract No. DE-AC02-06CH11357.

[1] D. J. Thouless, M. Kohmoto, M. P. Nightingale, and M. den Nijs, Quantized Hall conductance in a two-dimensional periodic potential, Phys. Rev. Lett. **49**, 405 (1982).

[2] F. D. M. Haldane, Model for a quantum Hall effect without Landau levels: Condensed-matter realization of the parity anomaly, Phys. Rev. Lett. **61**, 2015 (1988).

[3] Q. Niu, D. J. Thouless, and Y.-S. Wu, Quantized Hall conductance as a topological invariant, Phys. Rev. B **31**, 3372 (1985).

[4] C. L. Kane and E. J. Mele, Z_2 topological order and the quantum spin Hall effect, Phys. Rev. Lett. **95**, 146802 (2005).

[5] T. Fukui, Y. Hatsugai, and H. Suzuki, Chern numbers in discretized Brillouin zone: Efficient method of computing (spin) Hall conductances, J. Phys. Soc. Jpn. **74**, 1674 (2005).

[6] B. A. Bernevig, T. L. Hughes, and S.-C. Zhang, Quantum spin Hall effect and topological phase transition in HgTe quantum wells, Science **314**, 1757 (2006).

[7] L. Fu and C. L. Kane, Topological insulators with inversion symmetry, Phys. Rev. B **76**, 045302 (2007).

[8] L. Fu, C. L. Kane, and E. J. Mele, Topological insulators in three dimensions, Phys. Rev. Lett. **98**, 106803 (2007).

[9] J. E. Moore and L. Balents, Topological invariants of time-reversal-invariant band structures, Phys. Rev. B **75**, 121306(R) (2007).

[10] J. C. Y. Teo, L. Fu, and C. L. Kane, Surface states and topological invariants in three-dimensional topological insulators: Application to $Bi_{1-x}Sb_x$, Phys. Rev. B **78**, 045426 (2008).

[11] E. Prodan, Robustness of the spin-chern number, Phys. Rev. B **80**, 125327 (2009).

[12] K.-S. Lin, G. Palumbo, Z. Guo, J. Blackburn, D. Shoemaker, F. Mahmood, Z. Wang, G. Fiete, B. Wieder, and B. Bradlyn, Spin-resolved topology and partial axion angles in three-dimensional insulators, Nat. Commun. **15**, 550 (2024).

[13] K. G. Wilson, Confinement of quarks, Phys. Rev. D **10**, 2445 (1974).

[14] G. 't Hooft, A property of electric and magnetic flux in non-Abelian gauge theories, Nucl. Phys. B **153**, 141 (1979).

[15] I. Y. Aref'eva, Non-Abelian stokes formula, Theor. Math. Phys. **43**, 353 (1980).

[16] R. Yu, X. L. Qi, A. Bernevig, Z. Fang, and X. Dai, Equivalent expression of $\mathbb{Z}_2$ topological invariant for band insulators using the non-Abelian Berry connection, Phys. Rev. B **84**, 075119 (2011).

[17] L. Fidkowski, T. S. Jackson, and I. Klich, Model characterization of gapless edge modes of topological insulators using intermediate brillouin-zone functions, Phys. Rev. Lett. **107**, 036601 (2011).

[18] A. A. Soluyanov and D. Vanderbilt, Computing topological invariants without inversion symmetry, Phys. Rev. B **83**, 235401 (2011).

[19] A. Alexandradinata, X. Dai, and B. A. Bernevig, Wilson-loop characterization of inversion-symmetric topological insulators, Phys. Rev. B **89**, 155114 (2014).

[20] M. Taherinejad, K. F. Garrity, and D. Vanderbilt, Wannier center sheets in topological insulators, Phys. Rev. B **89**, 115102 (2014).

[21] D. Gresch, G. Autès, O. V. Yazyev, M. Troyer, D. Vanderbilt, B. A. Bernevig, and A. A. Soluyanov, Z2Pack: Numerical implementation of hybrid Wannier centers for identifying topological materials, Phys. Rev. B **95**, 075146 (2017).

[22] A. Alexandradinata and B. A. Bernevig, Berry-phase description of topological crystalline insulators, Phys. Rev. B **93**, 205104 (2016).

[23] A. Bouhon, A. M. Black-Schaffer, and R.-J. Slager, Wilson loop approach to fragile topology of split elementary band representations and topological crystalline insulators with time-reversal symmetry, Phys. Rev. B **100**, 195135 (2019).

[24] B. Bradlyn, Z. Wang, J. Cano, and B. A. Bernevig, Disconnected elementary band representations, fragile topology, and Wilson loops as topological indices: An example on the triangular lattice, Phys. Rev. B **99**, 045140 (2019).

[25] J. Ahn and B.-J. Yang, Unconventional majorana fermions on the surface of topological superconductors protected by rotational symmetry, Phys. Rev. B **103**, 184502 (2021).

[26] C. Fang, M. J. Gilbert, and B. A. Bernevig, Bulk topological invariants in noninteracting point group symmetric insulators, Phys. Rev. B **86**, 115112 (2012).

[27] S. Sur, A. C. Tyner, and P. Goswami, Mixed-order topology of Benalcazar-Bernevig-Hughes models, arXiv:2201.07205.

[28] M. B. Halpern, Field-strength and dual variable formulations of gauge theory, Phys. Rev. D **19**, 517 (1979).

[29] N. E. Bralić, Exact computation of loop averages in two-dimensional Yang-Mills theory, Phys. Rev. D **22**, 3090 (1980).

[30] P. Goddard and D. I. Olive, Magnetic monopoles in gauge field theories, Rep. Prog. Phys. **41**, 1357 (1978).

[31] A. C. Tyner, S. Sur, D. Puggioni, J. M. Rondinelli, and P. Goswami, Topology of three-dimensional dirac semimetals and quantum spin Hall systems without gapless edge modes, Phys. Rev. Res. **5**, L012019 (2023).

[32] W. A. Benalcazar, B. A. Bernevig, and T. L. Hughes, Quantized electric multipole insulators, Science **357**, 61 (2017).

[33] F. Schindler, A. M. Cook, M. G. Vergniory, Z. Wang, S. S. P. Parkin, B. A. Bernevig, and T. Neupert, Higher-order topological insulators, Sci. Adv. **4**, eaat0346 (2018).

[34] B. J. Wieder, Z. Wang, J. Cano, X. Dai, L. M. Schoop, B. Bradlyn, and B. A. Bernevig, Strong and fragile topological Dirac semimetals with higher-order Fermi arcs, Nat. Commun. **11**, 627 (2020).

[35] G. F. Lange, A. Bouhon, and R.-J. Slager, Subdimensional topologies, indicators, and higher order boundary effects, Phys. Rev. B **103**, 195145 (2021).

[36] A. Bouhon, G. F. Lange, and R.-J. Slager, Topological correspondence between magnetic space group representations and subdimensions, Phys. Rev. B **103**, 245127 (2021).

[37] Z. Wang, Y. Sun, X.-Q. Chen, C. Franchini, G. Xu, H. Weng, X. Dai, and Z. Fang, Dirac semimetal and topological phase transitions in A_3Bi (A = Na, K, Rb), Phys. Rev. B **85**, 195320 (2012).

[38] C. Le, X. Wu, S. Qin, Y. Li, R. Thomale, F.-C. Zhang, and J. Hu, Dirac semimetal in β-CuI without surface Fermi arcs, Proc. Natl. Acad. Sci. USA **115**, 8311 (2018).

[39] Z. Lin, C. Wang, P. Wang, S. Yi, L. Li, Q. Zhang, Y. Wang, Z. Wang, H. Huang, Y. Sun, Y. Huang, D. Shen, D. Feng, Z. Sun, J.-H. Cho, C. Zeng, and Z. Zhang, Dirac fermions in antiferromagnetic FeSn kagome lattices with combined space inversion and time-reversal symmetry, Phys. Rev. B **102**, 155103 (2020).

[40] B.-J. Yang and N. Nagaosa, Classification of stable three-dimensional Dirac semimetals with nontrivial topology, Nat. Commun. **5**, 1 (2014).

[41] N. Armitage, E. Mele, and A. Vishwanath, Weyl and Dirac semimetals in three-dimensional solids, Rev. Mod. Phys. **90**, 015001 (2018).

[42] E. V. Gorbar, V. A. Miransky, I. A. Shovkovy, and P. O. Sukhachov, Dirac semimetals $A_3Bi(a = Na, K, Rb)$ as $\mathbb{z}_2$ Weyl semimetals, Phys. Rev. B **91**, 121101(R) (2015).

[43] A. A. Burkov and Y. B. Kim, $\mathbb{z}_2$ and chiral anomalies in topological Dirac semimetals, Phys. Rev. Lett. **117**, 136602 (2016).

[44] M. Kargarian, M. Randeria, and Y.-M. Lu, Are the surface fermi arcs in Dirac semimetals topologically protected? Proc. Natl. Acad. Sci. U.S.A. **113**, 8648 (2016).

[45] G. Bednik, Surface states in Dirac semimetals and topological crystalline insulators, Phys. Rev. B **98**, 045140 (2018).

[46] M. Lin and T. L. Hughes, Topological quadrupolar semimetals, Phys. Rev. B **98**, 241103(R) (2018).

[47] E. Demler and S.-C. Zhang, Non-Abelian Holonomy of BCS and SDW quasiparticles, Ann. Phys. **271**, 83 (1999).

[48] F. Wilczek and A. Zee, Appearance of gauge structure in simple dynamical systems, Phys. Rev. Lett. **52**, 2111 (1984).

[49] See Supplemental Material at http://link.aps.org/supplemental/10.1103/PhysRevB.109.195149 for [give brief description of material].

[50] A. C. Tyner and P. Goswami, Spin-charge separation and quantum spin Hall effect of β-bismuthene, Sci. Rep. **13**, 11393 (2023).

[51] Z. Wang, H. Weng, Q. Wu, X. Dai, and Z. Fang, Three-dimensional Dirac semimetal and quantum transport in Cd_3As_2, Phys. Rev. B **88**, 125427 (2013).

[52] Z. K. Liu, B. Zhou, Y. Zhang, Z. J. Wang, H. M. Weng, D. Prabhakaran, S.-K. Mo, Z. X. Shen, Z. Fang, X. Dai, Z. Hussain, and Y. L. Chen, Discovery of a three-dimensional topological Dirac semimetal Na_3Bi, Science **343**, 864 (2014).

[53] S.-Y. Xu, C. Liu, S. K. Kushwaha, R. Sankar, J. W. Krizan, I. Belopolski, M. Neupane, G. Bian, N. Alidoust, T.-R. Chang, H.-T. Jeng, C.-Y. Huang, W.-F. Tsai, H. Lin, P. P. Shibayev, F.-C. Chou, R. J. Cava, and M. Z. Hasan, Observation of Fermi arc surface states in a topological metal, Science **347**, 294 (2015).

[54] Y. Du, B. Wan, D. Wang, L. Sheng, C.-G. Duan, and X. Wan, Dirac and Weyl semimetal in $XYBi$ (X = Ba, Eu; Y = Cu, Ag and Au), Sci. Rep. **5**, 14423 (2015).

[55] J. Xiong, S. K. Kushwaha, T. Liang, J. W. Krizan, M. Hirschberger, W. Wang, R. J. Cava, and N. P. Ong, Evidence for the chiral anomaly in the Dirac semimetal Na_3Bi, Science **350**, 413 (2015).

[56] S. K. Kushwaha, J. W. Krizan, B. E. Feldman, A. Gyenis, M. T. Randeria, J. Xiong, S.-Y. Xu, N. Alidoust, I. Belopolski, T. Liang *et al.*, Bulk crystal growth and electronic characterization of the 3D Dirac semimetal Na_3Bi, APL Mater. **3**, 041504 (2015).

[57] Q. D. Gibson, L. M. Schoop, L. Muechler, L. S. Xie, M. Hirschberger, N. P. Ong, R. Car, and R. J. Cava, Three-dimensional Dirac semimetals: Design principles and predictions of new materials, Phys. Rev. B **91**, 205128 (2015).

[58] A. Liang, C. Chen, Z. Wang, Y. Shi, Y. Feng, H. Yi, Z. Xie, S. He, J. He, Y. Peng, Y. Liu, D. Liu, C. Hu, L. Zhao, G. Liu, X. Dong, J. Zhang, M. Nakatake, H. Iwasawa, K. Shimada *et al.*, Electronic structure, Dirac points and Fermi arc surface states in three-dimensional Dirac semimetal Na_3Bi from angle-resolved photoemission spectroscopy, Chin. Phys. B **25**, 077101 (2016).

[59] H. Huang, S. Zhou, and W. Duan, Type-ii Dirac fermions in the $PtSe_2$ class of transition metal dichalcogenides, Phys. Rev. B **94**, 121117(R) (2016).

[60] C. Le, S. Qin, X. Wu, X. Dai, P. Fu, C. Fang, and J. Hu, Three-dimensional topological critical Dirac semimetal in $AMgBi(A = K, Rb, Cs)$, Phys. Rev. B **96**, 115121 (2017).

[61] T.-R. Chang, S.-Y. Xu, D. S. Sanchez, W.-F. Tsai, S.-M. Huang, G. Chang, C.-H. Hsu, G. Bian, I. Belopolski, Z.-M. Yu, S. A. Yang, T. Neupert, H.-T. Jeng, H. Lin, and M. Z. Hasan, Type-ii symmetry-protected topological Dirac semimetals, Phys. Rev. Lett. **119**, 026404 (2017).

[62] R. Kim, B.-J. Yang, and C. H. Kim, Crystalline topological Dirac semimetal phase in Rutile structure β'-PtO_2, Phys. Rev. B **99**, 045130 (2019).

[63] R. Yu, H. Weng, Z. Fang, X. Dai, and X. Hu, Topological node-line semimetal and Dirac semimetal state in antiperovskite cu_3PdN, Phys. Rev. Lett. **115**, 036807 (2015).

[64] J. P. Perdew, K. Burke, and M. Ernzerhof, Generalized gradient approximation made simple, Phys. Rev. Lett. **77**, 3865 (1996).

[65] G. Kresse and J. Furthmüller, Efficient iterative schemes for *ab initio* total-energy calculations using a plane-wave basis set, Phys. Rev. B **54**, 11169 (1996).

[66] G. Kresse and D. Joubert, From ultrasoft pseudopotentials to the projector augmented-wave method, Phys. Rev. B **59**, 1758 (1999).

[67] G. Pizzi, V. Vitale, R. Arita, S. Blugel, F. Freimuth, G. Géranton, M. Gibertini, D. Gresch, C. Johnson, T. Koretsune, J. Ibañez-Azpiroz, H. Lee, J.-M. Lihm, D. Marchand, A. Marrazzo, Y. Mokrousov, J. I. Mustafa, Y. Nohara, Y. Nomura, L. Paulatto *et al.*, Wannier90 as a community code: New features and applications, J. Phys.: Condens. Matter **32**, 165902 (2020).

[68] M. L. Sancho, J. L. Sancho, J. L. Sancho, and J. Rubio, Highly convergent schemes for the calculation of bulk and surface green functions, J. Phys. F: Met. Phys. **15**, 851 (1985).

[69] Q. Wu, S. Zhang, H.-F. Song, M. Troyer, and A. A. Soluyanov, Wanniertools: An open-source software package for novel topological materials, Comput. Phys. Commun. **224**, 405 (2018).

[70] A. Bouhon, Q. Wu, R.-J. Slager, H. Weng, O. V. Yazyev, and T. Bzdušek, Non-Abelian reciprocal braiding of Weyl points and its manifestation in ZrTe, Nat. Phys. **16**, 1137 (2020).

[71] J. Ahn and B.-J. Yang, Symmetry representation approach to topological invariants in $C_{2z}t$-symmetric systems, Phys. Rev. B **99**, 235125 (2019).

[72] B. Bradlyn, L. Elcoro, J. Cano, M. Vergniory, Z. Wang, C. Felser, M. Aroyo, and B. A. Bernevig, Topological quantum chemistry, Nature (London) **547**, 298 (2017).

[73] H. C. Po, A. Vishwanath, and H. Watanabe, Symmetry-based indicators of band topology in the 230 space groups, Nat. Commun. **8**, 1 (2017).

[74] J. Kruthoff, J. de Boer, J. van Wezel, C. L. Kane, and R.-J. Slager, Topological classification of crystalline insulators through band structure combinatorics, Phys. Rev. X **7**, 041069 (2017).

[75] E. Khalaf, H. C. Po, A. Vishwanath, and H. Watanabe, Symmetry indicators and anomalous surface states of topological crystalline insulators, Phys. Rev. X **8**, 031070 (2018).

[76] F. Tang, H. C. Po, A. Vishwanath, and X. Wan, Efficient topological materials discovery using symmetry indicators, Nat. Phys. **15**, 470 (2019).

[77] M. Vergniory, L. Elcoro, C. Felser, N. Regnault, B. A. Bernevig, and Z. Wang, A complete catalogue of high-quality topological materials, Nature (London) **566**, 480 (2019).

[78] F. Tang, H. C. Po, A. Vishwanath, and X. Wan, Comprehensive search for topological materials using symmetry indicators, Nature (London) **566**, 486 (2019).

[79] J. Cano, B. Bradlyn, Z. Wang, L. Elcoro, M. G. Vergniory, C. Felser, M. I. Aroyo, and B. A. Bernevig, Building blocks of topological quantum chemistry: Elementary band representations, Phys. Rev. B **97**, 035139 (2018).

[80] T. Zhang, Y. Jiang, Z. Song, H. Huang, Y. He, Z. Fang, H. Weng, and C. Fang, Catalogue of topological electronic materials, Nature (London) **566**, 475 (2019).

[81] L. Elcoro, B. J. Wieder, Z. Song, Y. Xu, B. Bradlyn, and B. A. Bernevig, Magnetic topological quantum chemistry, Nat. Commun. **12**, 5965 (2021).

[82] Y. Xu, L. Elcoro, Z.-D. Song, B. J. Wieder, M. Vergniory, N. Regnault, Y. Chen, C. Felser, and B. A. Bernevig, High-throughput calculations of magnetic topological materials, Nature (London) **586**, 702 (2020).

[83] M. G. Vergniory, B. J. Wieder, L. Elcoro, S. S. P. Parkin, C. Felser, B. A. Bernevig, and N. Regnault, All topological bands of all nonmagnetic stoichiometric materials, Science **376**, eabg9094 (2022).